Quaternary Research
Copyright © University of Washington. Published by Cambridge University Press, 2020.
doi:10.1017/qua.2020.7

Glacial events during the last glacial termination in the Pagele valley, Qiongmu Gangri peak, southern Tibetan Plateau, and their links to oceanic and atmospheric circulation

Xiangke Xu[a,b]*, Tandong Yao[a,b], Baiqing Xu[a,b], Chaolu Yi[a,b], Yong Sun[a,c], Xuezhen Zeng[a,c], Guocheng Dong[d], Baolin Pan[e]

[a]Key Laboratory of Tibetan Environment Changes and Land Surface Processes, Institute of Tibetan Plateau Research, CAS, Beijing 100101, China
[b]CAS Center for Excellence in Tibetan Plateau Earth Science, Beijing 100101, China
[c]University of Chinese Academy of Sciences, Beijing 100049, China
[d]State Key Laboratory of Loess and Quaternary Geology, Institute of Earth Environment, Chinese Academy of Sciences, Xi'an 710061, China
[e]College of Resources, Environment and Tourism, Capital Normal University, Beijing 100048, China
*Corresponding author at: Key Laboratory of Tibetan Environment Changes and Land Surface Processes, Institute of Tibetan Plateau Research, CAS Center for Excellence in Tibetan Plateau Earth Science, Beijing 100101, China. E-mail address: xkxu@itpcas.ac.cn (X. Xu).

(Received August 5, 2019; Accepted January 12, 2020)

Abstract

During the last glacial termination, a warming trend was generally interrupted by rapid millennium-scale cold reversals, such as the Greenland (Isotope) Stadial 1 (GS-1) and GS-2a events. To understand how glaciers on the Tibetan Plateau (TP) responded to these rapid climate events, this study constrained the timing and extent of three glacial events during the late-glacial period. Specifically, using a cosmogenic ^{10}Be exposure dating method, we dated three prominent glacial moraines (PM1, PM2, PM3) back to 15,850 ± 980, 14,140 ± 880, and 12,430 ± 790 yr in the Pagele valley, southern TP, corresponding to GS-2a, Greenland Interstadial 1 (GI-1), and GS-1, respectively. By simulating glacial extents forced by different climate scenarios, the study constrained the temperature decreases relative to present to be 2.6°C–2.9°C, ∼1.6°C, and 1.4°C–1.5°C during the GS-2a, GI-1, and GS-1 periods in the region, with precipitation values of 60%–80%, ∼100%, and 80%–90% of present value, respectively. Considering information from oceanic and atmospheric circulation, the study suggested that on the TP, the glacial events during the last glacial termination were well connected with the millennium-scale climate events in the North Atlantic region through the westerlies, while the Indian summer monsoon played a positive role in sustaining the glaciers under the warming climate trend.

Keywords: Last glacial termination; Glacial event; Cosmogenic ^{10}Be dating; Millennium-scale climate events; Pagele valley

INTRODUCTION

The last glacial termination is a global climate transition phase from the last glacial maximum (LGM) to full Holocene conditions. It may represent the largest readjustments of the Earth's natural climate over the past 100,000 yr (Broecker and van Donk, 1970; Denton et al., 2010). During this interval, a warming trend was generally interrupted by rapid millennium-scale cold reversals, such as the Greenland (Isotope) Stadial 1 (GS-1, Younger Dryas) and GS-2a (Heinrich 1) events (Björck et al., 1998; Rasmussen et al., 2006). This may have induced pauses in glaciers retreating from their LGM limits and even glacial readvances, so the period is usually called the "late-glacial" period. Currently, it is far from clear how glaciers responded to these cold climate reversals. For example, we are not sure how many glacial stillstands and/or advances occurred during this period in different North Hemisphere (NH) regions. Constraining the timing of these glacial events can therefore help us recognize the processes contributing to the last glacial termination and understand the role of millennial-scale climate events in adjusting glacial extents.

Mountain glaciers are sensitive to regional and local climate change, and thus glacial records are usually used to retrieve past climatic change (Thompson et al., 1997; Thackray et al. 2008). Former glacial extents, marked by lateral and terminal moraines along with erosional trimlines, reflect spatial and temporal changes of glacial mass balance that are

Cite this article: Xu, X., Yao, T., Xu, B., Yi, C., Sun, Y., Zeng, X., Dong, G., Pan, B. 2020. Glacial events during the last glacial termination in the Pagele valley, Qiongmu Gangri peak, southern Tibetan Plateau, and their links to oceanic and atmospheric circulation. *Quaternary Research* 95, 129–141. https://doi.org/10.1017/qua.2020.7

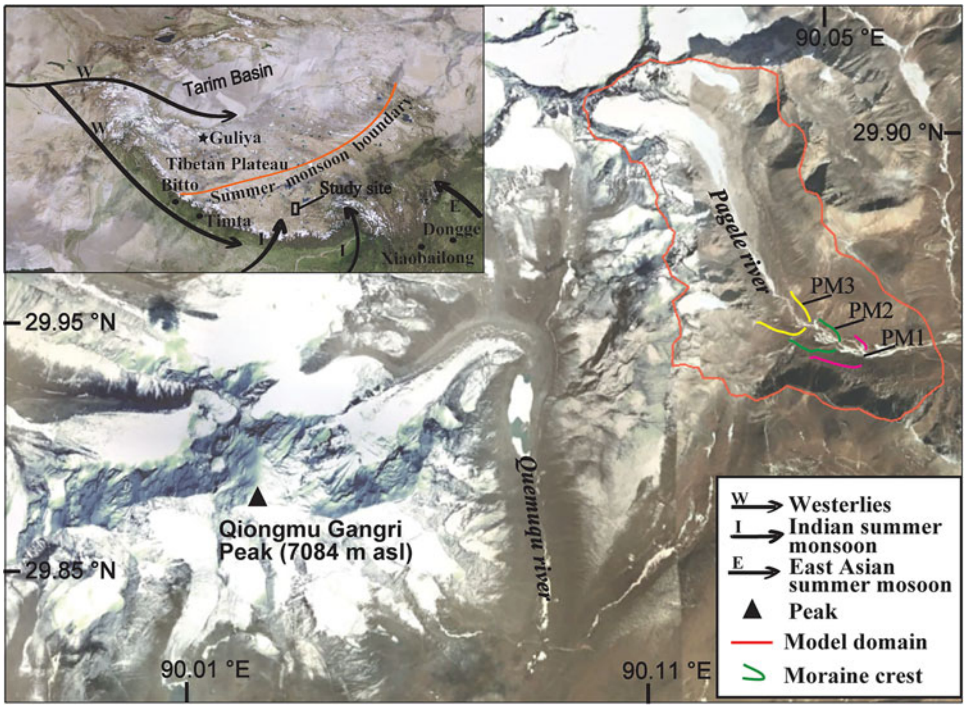

Figure 1. Google Earth map showing the location of the Pagele valley, Qiongmu Gangri peak in the southern Tibetan Plateau (TP). The inset shows the main atmospheric circulation systems operating on the TP. Note that the PM1, PM2, and PM3 moraine crests are delineated by dark pink, green, and yellow lines, respectively. (For interpretation of the references to color in this figure legend, the reader is referred to the web version of this article.)

mainly influenced by climatic conditions (Cuffey and Paterson, 2010). Therefore, paleoclimatic inferences can be made by reconstructing the timing and extent of past mountain glaciers.

As the most prominent topographic feature across the middle to low latitudes in Asia, the Tibetan Plateau (TP) rises to a mean elevation of more than 4000 m above sea level (m asl), with an area of 2.5 million km^2 (Zhang et al., 2002). Its uplift has great impact on atmospheric circulations, initiating the Asian monsoons and splitting the westerlies of the NH into two branches (Prell and Kutzbach, 1992; Raymo and Ruddiman, 1992; Benn and Owen, 1998). Such geographic features make the plateau a distinctive connection to global and regional climate (Molnar and England, 1990; Benn and Owen, 1998; Zheng et al., 2002). Understanding the timing and features of late-glacial events on the TP is therefore important, because it can yield information on climate evolution during the last glacial termination.

Throughout the TP, cosmogenic ^{10}Be exposure dating has been widely used to define the timing of glaciations (e.g., Owen et al., 2008; Chevalier et al., 2011; Heyman et al., 2011). A few examples of late-glacial moraines have been identified using the cosmogenic ^{10}Be dating method (Owen and Dortch, 2014; Heyman, 2014). However, relative to the LGM and other glaciations, such as Marine Isotopic Stage 4 (MIS 4) and MIS 3 (e.g., Owen et al., 2008; Dortch et al., 2013; Murari et al., 2014), reliable chronological evidence of the millennium-scale glacial events in the late-glacial period is still scarce. Moreover, little work has been done to quantitatively reconstruct glacier–climate conditions for the late-glacial period on the TP.

Our study focuses on the dating and modeling of the late-glacial glacial events in the region of Qiongmu Gangri peak, which lies at the westernmost margin of the west Nyaiqentanggulha Mountains (Fig. 1). Situated in the transition zone that is dominated by the westerlies during the winter and spring and by the Indian summer monsoon during the summer and fall (Yao et al., 2013), the region is well suited for assessing glacial response to these two climate systems. The landforms of the Qiongmu Gangri peak afford a record of glacial activities since the last glacial (Dong et al., 2017). Here we present a ^{10}Be exposure chronology of moraines that documents the timing of late-glacial glacial events in the Pagele valley on the eastern slope of the Qiongmu Gangri peak. In the valley, the main glacier terminates at an elevation of 5470 m asl and has a length of 2500 m. To infer the past climate that prevailed in the last glacial termination from the glacial geomorphological record, we use a coupled glacial mass-balance and ice-flow model to generate a glacier–climate reconstruction for the late-glacial glacial events in the Pagele valley.

METHODS

Geomorphology and ^{10}Be sampling method

In the Qiongmu Gangri peak region, the LGM end moraines are prominent and are located at tributary valley mouths with

https://doi.org/10.1017/qua.2020.7 Published online by Cambridge University Press

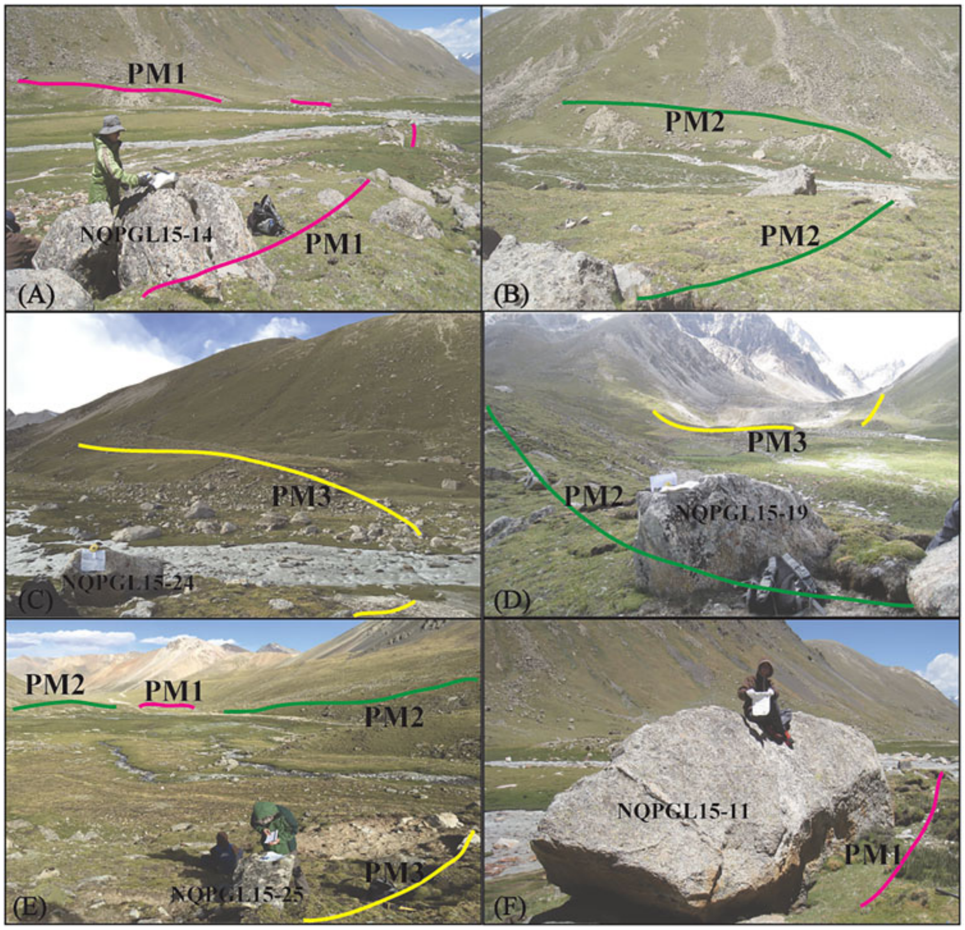

Figure 2. Photographic views for the PM1, PM2, and PM3 moraines. (A) Field photo for the PM1 moraine with one of the sampled boulders in the foreground, as viewed looking northeast on the moraine crest; (B) the PM2 moraine with boulders on it, as viewed looking north on the moraine crest; (C) the PM3 moraine with one of the sampled boulders in the left lower corner of the photo, as viewed looking northwest on the moraine; (D) field photo showing the relative position of the PM2 and PM3 moraines, as viewed looking northwest on the PM2 moraine crest; (E) the relative position photo for the PM1, PM2, and PM3, as viewed looking southeast on the PM3 moraine; (F) a typical boulder sampled for ^{10}Be exposure dating on the PM1. Note that the PM1, PM2, and PM3 moraine crests are delineated by dark pink, green, and yellow lines on the photos, respectively. (For interpretation of the references to color in this figure legend, the reader is referred to the web version of this article.)

an elevation of ~4800 m asl. The LGM lateral moraines can be traced upvalley to an elevation of ~5100 m asl (Dong et al., 2017). Inside the LGM moraines to the modern glaciers, several post-LGM moraine loops and remnants can be found, but the numbers of these post-LGM moraines are very different between valleys. We chose the Pagele valley as a ^{10}Be sampling target, because eight moraine loops can be clearly found above 5100 m asl in the valley. This offers great potential to collect samples to study the millennium-scale cold reversals in the last glacial termination. In this study, we focus on the three outermost moraine sets that were most likely formed by late-glacial glacial events in the valley (Figs. 2 and 3). We named the three moraine sets PM1, PM2, and PM3 from outer (older) to inner (younger). The lithology of the clasts on the three moraines is very similar and consists of schist, gneiss, and granitic diorite. Although the three moraine sets are incised by a river, the loop shapes can be traced in the field. The PM1, terminating at an elevation of 5170 m asl, is the most discontinuous moraine, mainly due to the longtime river incision. It is covered by a 5- to 10-cm-thick soil layer with thin grass-topped turf. Glacial boulders, with diameters of up to 1.5 m, protrude on the moraine surface. These boulders commonly present slight weathering characteristics with knobs and cavernous pits on their surfaces. Upvalley to about 500 m, there is the second moraine set of PM2, rising 10–15 m above the riverbed. The lateral-frontal moraine PM2 terminates at an altitude of 5200 m asl and can be traced to an elevation of 5250 m asl. Some patches of soil, along with sparse vegetation, have also developed on this moraine. The boulders on the moraine set are larger than those on PM1, with the largest having a diameter of ~3 m. PM3 has features similar to PM2 but terminates at a slightly higher elevation of 5230 m asl. The positions of the three moraines indicate that the glacier retreated 900–1000 m from the PM1 to PM3, and the glacier's length at the PM1 position was 3500 m longer than the modern glacier.

About 0.5 kg of rock samples for the ^{10}Be exposure dating was chiseled from the upper surfaces of quartz-rich boulders

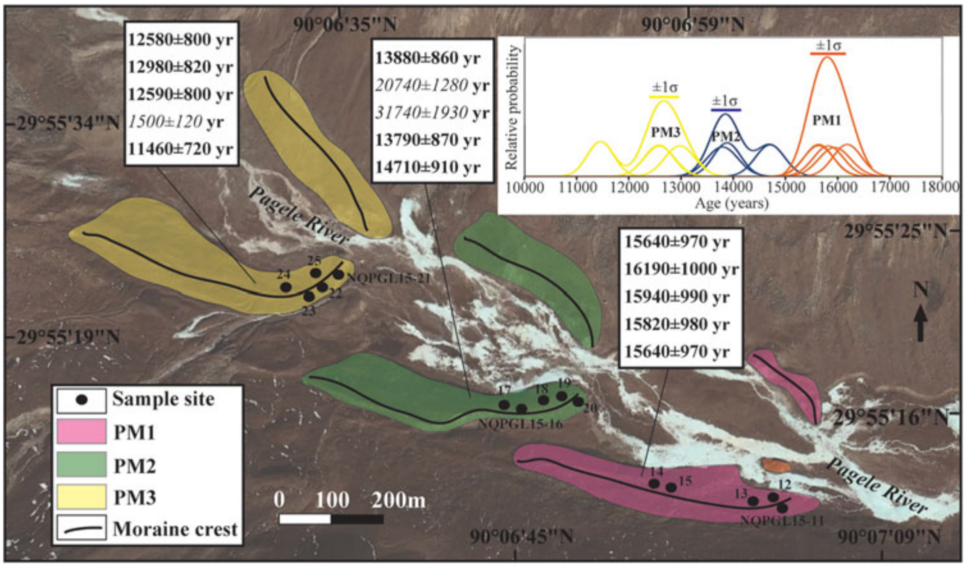

Figure 3. (color online) Geomorphological mapping for the PM1, PM2, and PM3 moraine from Google Earth map and cosmogenic ^{10}Be dating results for the three moraine sets in the Pagele valley. Note that the age values in italics are outliers in each group. The inset shows plots of probability density function (PDF) for the ^{10}Be exposure ages on the PM1, PM2, and PM3 moraines. Individual ages are plotted as a normal distribution (PDF) using the exposure age and its internal uncertainty. The cumulative PDFs are made by summing individual-age PDFs on the same moraines. The uncertainty bar (±1σ) represents the mean of internal uncertainties of the individual ages from the same moraine.

on the three moraine sets (Supplementary Figs. S1–S3). Sampling locations were targeted on the moraine crests to avoid the likelihood of burial/exhumation histories and slope instability. To reduce the possibility that the boulders and rock surfaces may have been covered with snow for significant periods (several months per year) or were previously covered with sediment, the highest parts of the largest boulders were chosen for sampling. Five samples from each of the moraine sets were sampled to check the reproducibility of the dating results and the possibility of the ^{10}Be inheritance by prior exposure. Each sample location was measured using a handheld GPS, and the size of each boulder was also recorded. The surrounding conditions were photographed to document the position and geomorphic features for each sampling site. Cosmic-ray shielding by topography was calculated using the codes from Li (2013) on the 30-m ASTER DEM. No corrections were made for erosion or snow coverage.

^{10}Be exposure dating method

Sample processing and ^{10}Be measurements were conducted at Xi'an Accelerator Mass Spectrometry (Xi'an-AMS) Center, Institute of Earth Environment, Chinese Academy of Sciences. Quartz purification, Be separation, and cathode preparation were carried out following the methods of Kohl and Nishiizumi (1992) and Dortch et al. (2009). The ^{10}Be/^{9}Be ratios were measured by AMS with normalization to the revised ^{10}Be ICN standard with ^{10}Be/^{9}Be ratio of 2.851×10^{-12} (Nishiizumi et al., 2007).

For each ^{10}Be sampling set from the same moraines, one blank sample was used to correct the measured isotope ratios, which were then converted to ^{10}Be concentrations for age calculations in the next step. We calculated the ages for three scaling models using CRONUS-Earth online calculators (version 3; Balco et al., 2008; http://hess.ess.washington.edu, December, 2018). The sample ages are presented in Table 1, with external (analytical and production rate uncertainty) and internal (analytical uncertainty only) uncertainties at 1σ. Based on analytical approximations to modeled fluxes of main atmospheric cosmic-ray particles responsible for in situ cosmogenic nuclide production, the LSDn model by Lifton et al. (2014) predicts realistic atmospheric cosmic-ray fluxes. It works well at low-latitude and high-altitude sites like our study area. Also, the model has fewer systematic age uncertainties than the St and Lm (time-independent and time-dependent) models of Lal (1991) and Stone (2000). We therefore chose to use the exposure ages from the LSDn scaling model when discussing chronology in the paper. Furthermore, to statistically test whether there are outliers in an age group from one moraine, this study uses Peirce's criterion (Peirce, 1852) following the procedure of Blomdin et al. (2016).

Glacial modeling method

This study used a glacial model to reconstruct the ice thickness and to invert the paleoclimate conditions from the three sets of moraines. The model couples a two-dimensional glacial mass-balance model to a shallow ice-approximation ice-flow model, which is fully described by Plummer and Phillips (2003). This model takes into account the topographic and atmospheric controls on energy and mass of

Table 1. Cosmogenic ^{10}Be exposure dating results on the moraines of PM1 (NQPGL15-11 to NQPGL15-15), PM2 (NQPGL15-16 to NQPGL15-20), and PM3 (NQPGL15-21 to NQPGL15-25), with the age values in italics being outliers in each group.

							St [a]			Lm [b]			LSDn [c]		
Sample ID	Latitude (°N)	Longitude (°E)	Elevation (m asl)	Sample thickness (cm)	Shielding correction factor	^{10}Be concentration ($\times 10^5$ atom/g SiO_2)	Age (years)	Internal error (years)	External error (years)	Age (years)	Internal error (years)	External error (years)	Age (years)	Internal error (years)	External error (years)
NQPGL15-11	29.9202	90.1173	5163	2.7	0.979233	11.89 ± 0.22	15,850	290	1290	15,880	290	1230	15,640	290	970
NQPGL15-12	29.9202	90.1172	5167	2.2	0.978911	12.37 ± 0.21	16,410	280	1330	16,390	280	1270	16,190	280	1000
NQPGL15-13	29.9202	90.1175	5166	2.1	0.979363	12.21 ± 0.23	16,180	310	1320	16,200	310	1260	15,940	310	990
NQPGL15-14	29.9198	90.1160	5133	2.5	0.978709	11.88 ± 0.22	16,040	290	1310	16,070	300	1250	15,820	290	980
NQPGL15-15	29.9199	90.1163	5135	2.6	0.978929	11.74 ± 0.21	15,850	280	1290	15,880	280	1230	15,640	280	970
NQPGL15-16	29.9213	90.1135	5206	3.9	0.980779	10.44 ± 0.20	13,770	260	1120	14,060	270	1090	13,880	260	860
NQPGL15-17	29.9211	90.1131	5212	2.9	0.980769	16.71 ± 0.28	*21,850*	*370*	*1770*	*21,010*	*360*	*1620*	*20,740*	*350*	*1280*
NQPGL15-18	29.9210	90.1129	5217	2.5	0.98099	27.30 ± 0.36	*35,620*	*470*	*2880*	*32,840*	*440*	*2520*	*31,740*	*420*	*1930*
NQPGL15-19	29.9211	90.1128	5220	3.6	0.981227	10.41 ± 0.22	13,610	290	1120	13,930	300	1090	13,790	300	870
NQPGL15-20	29.9211	90.1133	5218	3.7	0.980603	11.21 ± 0.21	14,700	280	1200	14,900	280	1160	14,710	280	910
NQPGL15-21	29.9228	90.1098	5237	2.5	0.983835	9.32 ± 0.21	11,950	270	980	12,640	280	990	12,580	280	800
NQPGL15-22	29.9228	90.1098	5237	2.1	0.983835	9.80 ± 0.22	12,530	280	1030	13,080	290	1030	12,980	290	820
NQPGL15-23	29.9228	90.1097	5237	2.8	0.982976	9.30 ± 0.21	11,960	280	990	12,650	290	1000	12,590	290	800
NQPGL15-24	29.9237	90.1096	5241	3.1	0.982782	1.01 ± 0.05	*1300*	*70*	*120*	*1490*	*80*	*140*	*1500*	*80*	*120*
NQPGL15-25	29.9233	90.1095	5239	4.2	0.984704	8.23 ± 0.18	10,680	240	880	11,510	260	900	11,460	250	720

[a]Time-independent production scaling model by Lal (1991) and Stone (2000).
[b]Time-dependent production scaling model by Lal (1991) and Stone (2000).
[c]Production scaling model by Lifton et al. (2014).

the glacial surface, including explicitly incoming solar radiation, air humidity, wind speed, cloudiness, and snow avalanching on steep hillslopes. It therefore allows us to explicitly quantify the topographic shading and consider the impact of albedo on ice melting. We used the model to calculate the glacial mass balance at a monthly time step to get annual net mass balance. The calculated net mass balances were then input to the shallow ice-approximation ice-flow model, which was run iteratively until the calculated ice thickness attained a steady state.

The model domain was defined by a digital elevation model (DEM) with 30 m × 30 m grids, which was downloaded from the Geospatial Data Cloud (http://www.gscloud.cn, July, 2018). Modern glacial thickness data were adopted from Farinotti et al. (2019) and subtracted from the DEM to generate the ice-free topography on which the model ran. The model was forced by monthly mean meteorological data over the 1981–2016 period from the Dangxiong Station (30°29′N, 91°06′E, 4200 m asl), the long-term observational station nearest to the Pagele valley. To scale the monthly temperature and precipitation with elevation, we used the regional values of temperature lapse rates and precipitation gradients from Xu et al. (2017a). Monthly mean climate variables from the Dangxiong Station, as a reference for the glacier–climate modeling, are listed in Supplementary Table S1. Due to the large uncertainty in albedo and its dominant impact on energy, and thus net mass ablation calculation, we calibrated this parameter in an effort to match simulated glaciers with the observed modern glaciers in the Pagele valley. After multiple simulations with different albedo values, we confirmed that when the low and high albedos were 0.2 and 0.7, respectively, the simulated glaciers were well matched with the observed ones (Fig. 4). We therefore used the two values as optima in the following simulations. A full description of the model inputs is given in Supplementary Table S2. By altering temperature and precipitation from contemporary conditions (hereafter referred to as ΔT, temperature change relative to present; F_p, precipitation as fractional value relative to modern), we ran the model iteratively until the simulated glaciers fit well with their corresponding moraine positions.

RESULTS AND DISCUSSION

^{10}Be exposure dating

In total we dated 15 boulder samples for the three moraine sets of PM1, PM2, and PM3. All of these ^{10}Be ages are listed in Table 1 and Figure 3. Five samples from the PM1 moraine (NQPGL15-11 to NQPGL15-15) present ages ranging from 15,640 to 16,190 yr with an uncertainty-weighted mean age of 15,850 ± 980 yr. These ages cluster tightly and overlap with each other within 1σ internal uncertainty. The PM2 samples have five ages (NQPGL15-16 to NQPGL15-20) that constitute a wide spread from 13,790 to 31,740 yr. The two ages of 20,740 and 31,740 yr (NQPGL15-17 and NQPGL15-18) are identified as outliers by the Peirce's test, and they are too old to represent the timing when the PM2 moraine was abandoned by the Pagele glacier. The two older samples can be explained by ^{10}Be inheritance (exposed before they were deposited on the moraine PM2). Excluding the two oldest ages (as outliers), three ages (NQPGL15-16, NQPGL15-18, and NQPGL15-20), however, are statistically indistinguishable within 1σ external uncertainty and have an uncertainty-weighted mean age of 14,140 ± 880 yr. For the PM3 moraine, five ^{10}Be ages (NQPGL15-21 to NQPGL15-25) range from 1490 to 12,980 yr. The youngest age of 1490 yr (NQPGL15-24) is obviously an outlier of this group of ages (the boulder was most likely exhumed) and can be excluded when interpreting the age of the PM3 moraine. The remaining four ages overlap with each other within 1σ external uncertainty with an uncertainty-weighted mean age of 12,430 ± 790 yr. Collectively, excluding the outliers, the PM1, PM2, and PM3 ages are statistically distinguishable from each other based on the age probability peaks (fig. 3), and the three groups of ages are consistent with the morphostratigraphic features. This means we can confidently constrain the timing of the late-glacial glacial events using these ages from the respective PM1, PM2, and PM3 moraines.

Two scenarios have been generally applied to interpret the multiple cosmogenic ^{10}Be ages from one moraine. One uses the mean of the multiple boulder ^{10}Be ages to represent the timing when moraines were abandoned by glaciers (e.g., Schaefer et al., 2009; Young et al., 2019). This scenario assumes that the moraine surfaces remained stable after they formed and that inheritance of ^{10}Be is as important as postdepositional shielding in its effect on sample ages (Chevalier et al., 2011). The other scenario considers the oldest ages as the timing when moraine surfaces were exposed (e.g., Zech et al., 2009; Heyman, 2014). This scenario assumes that the dated boulders are likely to be exhumed to moraine surfaces and/or rotated by postdepositional movement, considering the fact that moraine surfaces are unlikely to remain stable after their formation (Heyman et al., 2011). However, our ^{10}Be ages from each of the three moraines cluster tightly at most within a ∼1000 yr range after the ^{10}Be age outliers are excluded. This allows us to correlate the moraines to the millennial-scale climate events during the last glacial termination. Therefore, regardless of the mean (15,850 ± 980, 14,140 ± 880, and 12,430 ± 790 yr) and the oldest ages (16,190 ± 1000, 14,710 ± 910, and 12,980 ± 820 yr) from each of the three moraines, they all suggest that the PM1, PM2, and PM3 moraines respectively correspond well to the GS-2a (or Heinrich 1, 16.9–14.7 ka), GI-1 (or Bølling-Allerød, 14.7–12.7 ka), and GS-1 (or Younger Dryas, 12.7/12.9–11.5/11.7 ka) events in the Greenland ice-core record (Björck et al., 1998; Rasmussen et al., 2006; Ressen and Isarin, 2001).

GS-2a and GS-1 glacial events have also been reported in other valleys of the west Nyaiqentanggulha Mountains. At the eastern margin of the west Nyaiqentanggulha Mountains, Owen et al. (2005) reported a late-glacial moraine that is a latero-frontal moraine and terminates at an elevation of

https://doi.org/10.1017/qua.2020.7 Published online by Cambridge University Press

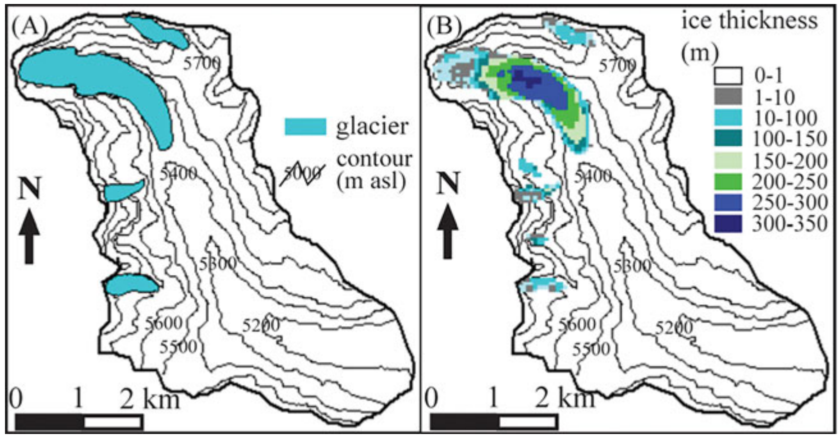

Figure 4. (color online) Comparison of the glacial distribution for observed (A) and modeled (B) glaciers under modern climate conditions in the Pagele valley.

~4920 m asl, 3300 m away from the modern glacier. They collected four boulder samples for cosmogenic ^{10}Be dating from the moraine crest and dated the moraine back to 15,900 ± 900 yr (mean age). Using the same method in our study, we recalculated the ages for the four samples (Supplementary Table S3). The recalculated ages range from 15,540 ± 1050 to 17,900 ± 1220 yr (±1σ external uncertainty), with an uncertainty-weighted mean age of 16,640 ± 1110 yr using the LSDn scaling model of Lifton et al. (2014). Closer to our study site, Chevalier et al. (2011) also dated a late-glacial moraine set (YanBaJian inner moraine) that is located at an elevation of ~5300 m asl, with a distance about 3000 m from the modern glacier. Five boulder ^{10}Be samples dated the YanBaJian inner moraine back to 11,000 ± 2000 yr after one outlier was rejected (Chevalier et al., 2011). We also recalculated the ages for these five samples and found that the ages are between 11,850 ± 740 and 21,300 ± 1320 yr using our scaling assumptions. After outlier evaluation by Peirce's criterion (Blomdin et al., 2016), we identified two outliers (15,350 ± 960 and 21,300 ± 1320 yr). Rejecting the outliers, the remaining ages have an uncertainty-weighted mean age of 12,830 ± 810. These recalculated moraine ^{10}Be ages are comparable to our ^{10}Be ages for the PM1 and PM3 and thus suggest that the GS-2a and GS-1 glacial events occurred in the west Nyaiqentanggulha Mountains. We note that this is the first time that the chronology for the GI-1 glacial event in the region has been reported, making it impossible to correlate the corresponding ages to other sites.

Glacial modeling

To establish the climate scenarios that support the glacial geometries constrained by the PM1, PM2, and PM3 moraines, we set the F_p to be from 0.6 to 1.4 with an incremental change of 0.1, and found the corresponding ΔTs that can force the model to produce the respective glacial extents (Fig. 5). Without precipitation change, the respective glacial extents for PM1, PM2, and PM3 required temperatures 1.9°C, 1.6°C, and 1.2°C lower than present, meaning the glacier

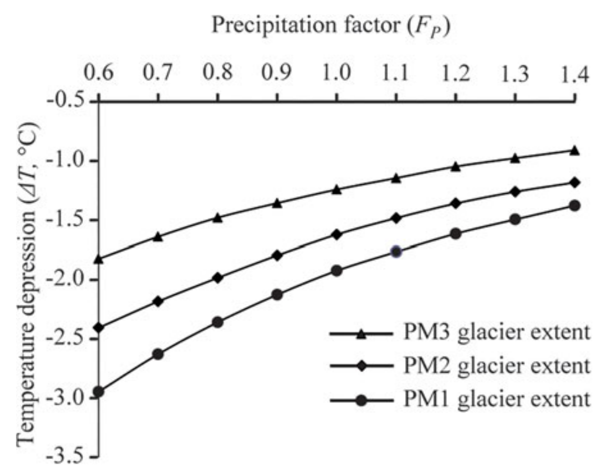

Figure 5. Plots of the temperature and precipitation combinations (ΔT–F_p) that yield the GS-1, GI-1, and GS-2a glacial extents, which match the PM3, PM2, and PM1 moraine positions, respectively.

is more sensitive to the temperature in wetter conditions than in drier conditions. For example, under precipitation of 30% more than the present (F_p = 1.3), 0.5°C of warming is needed to simulate the glacial retreat from the PM1 to PM3; but under the precipitation of 30% less than the present (F_p = 0.7), 1.0°C of warming is needed to simulate the same retreat. For each glacial extent, varying the precipitation by 10% in the wetter conditions can be compensated by a 0.1°C–0.2°C change in temperature; but in the drier conditions, a 0.3°C–0.4°C temperature change is required.

Figure 5 displays all ΔT–F_p climate scenarios that can force the model to produce each of glacial extents constrained by the PM1, PM2, and PM3 moraines. Under these scenarios, the reproduced glaciers have areas of about 12.6, 11.6, and 10.9 km^2 for the PM1, PM2, and PM3 moraines, respectively. For the PM1 glacial extent, however, the modeled glacial volumes range from 1.03 to 1.14 km^3, and the maximum ice thicknesses vary from 397 to 424 m, with larger volumes and ice thicknesses in the wetter conditions. The glacial

https://doi.org/10.1017/qua.2020.7 Published online by Cambridge University Press

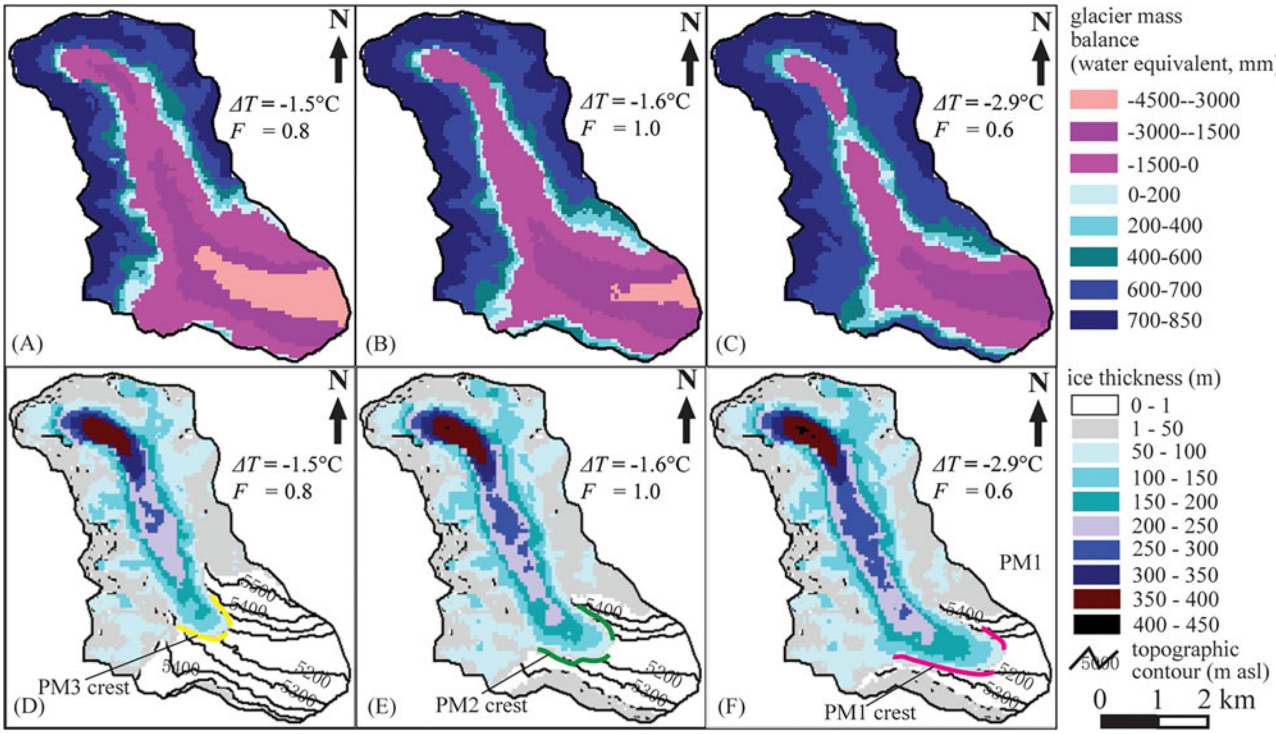

Figure 6. (color online) Simulations of the GS-1, GI-1, and GS-2a glacial mass balances and extents in the Pagele valley under the ΔT–F_p combinations of −1.5°C–0.8 (A, D), −1.6°C–1.0 (B, E), and −2.9°C–0.6 (C, F), respectively. Note that the GS-1, GI-1, and GS-2a glacial limits (PM3, PM2, and PM1 moraine positions) are also shown for comparison.

equilibrium line altitudes (ELAs) under these ΔT–F_p conditions for PM1 are between ~5400 and ~5440 m, with lower values under cooler conditions. The successful ΔT–F_p scenarios reproduce the glacial volumes varying from 0.79 to 0.88 km^3 for the PM2 moraine, and from 0.61 to 0.68 km^3 for the PM3 moraine. The modeled maximum ice thicknesses range from 386 to 402 m and from 376 to 387 m for the PM2 and PM3 moraines, respectively. The modeled ELAs for PM2 and PM3 vary from ~5460 to ~5490 m and from ~5510 to ~5540 m, respectively. Figure 6 demonstrates the modeled net annual mass balance and corresponding ice thickness for each of the three glacial events under three ΔT–F_p combinations of −2.9°C–0.6, −1.6°C–1.0, and −1.5°C–0.8, respectively, and the corresponding ELAs are ~5420, ~5480, and ~5530 m under these three climate scenarios.

When interpreting the paleoclimates based on the model results, we assume that the ΔT–F_p combinations in Figure 5 are the only possible scenarios for the three glacial events. Uncertainties exist in these combinations due to potential uncertainties in the model input climate data and biases in the calculations. These include the altitudinal gradients of monthly mean temperature and precipitation, which are based on a small number of weather stations, and estimates of second-order climate data that are not available locally (e.g., wind speed, relative humidity). In addition, our lack of knowledge of how much these second-order climate variables differed during the last glacial termination also adds uncertainty to the modeled ΔT–F_p combinations. Although we do not evaluate the uncertainties caused by those effects, previous studies have suggested that errors due to limited input data produce uncertainties in the ΔT and F_p of about ± 0.5°C and ± 0.3, respectively (e.g., Plummer, 2002; Laabs et al., 2006; Xu et al., 2013). As this investigation used a method similar to these studies, we believe that the uncertainties in our estimated ΔT and F_p are not beyond these values. In addition, our study did not account for impacts of debris cover on the paleoclimate inferences due to lack of measurements of debris cover on the modern glacier. A thin supraglacial debris cover enhances glacial melting by reducing surface albedo and increasing the absorption of the incident heat, whereas a thick debris cover can protect the glacier from melting by insulating the surface. Which impact is dominant depends on a critical thickness (1–10 cm) of the debris cover (e.g., Lana et al. 1997; Pu et al. 2003; Nicholson and Benn, 2006; Mihalcea et al., 2008). Considering the debris cover promotes glacial ablation, the inferred ΔT (temperature reduction in our study) would be overestimated by the glacial model (using a lower albedo value). In contrast, the inferred ΔT would be underestimated if the debris cover was thicker than the critical thickness. Furthermore, there are no data to quantify the highly variable distribution of debris on the glacier's surface and how this differs between modern and past glaciers. This makes it difficult to precisely evaluate the impact of debris cover on the paleoclimate inferences.

For the three glacial events, no unique paleoclimate solution can be found in our model experiment results (three ΔT–F_p combination curves). The estimates of ΔT–F_p combinations shown in Figure 5 are the only possible climate

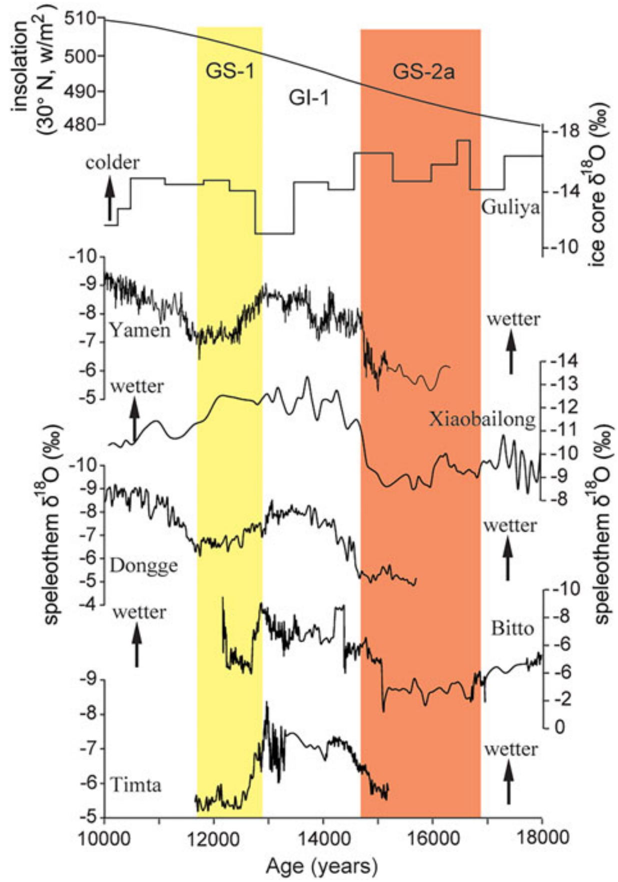

Figure 7. Time series of summer insolation at 30°N (Berger and Loutre, 1991) and $\delta^{18}O$ record from Guliya ice core on the northwestern Tibetan Plateau (Thompson et al., 1997) as proxies for temperature change, and Indian summer monsoon speleothem $\delta^{18}O$ records from Dongge, Yamen, Xiaobailong, Timta, and Bitto caves (Yuan et al., 2004; Sinha et al., 2005; Yang et al., 2010; Cai et al., 2015; Kathayat et al., 2016) as proxies for precipitation variability in the region. The yellow and orange rectangles denote the GS-1 (12.9–11.7 ka) and GS-2a (16.9–14.7 ka) glacial stages, respectively, between which is the GI-1 period (14.6–13.0 ka; Björck et al., 1998; Rasmussen et al., 2006). (For interpretation of the references to color in this figure legend, the reader is referred to the web version of this article.)

scenarios. To better constrain the ranges of the ΔT and F_p, we have to reference other independent climate proxies. Oxygen isotopic ratios (denoted as $\delta^{18}O$) have been used extensively in reconstructions of long-term averaged air temperature (ice-core $\delta^{18}O$ records) and Asian monsoon intensity (cave speleothem $\delta^{18}O$ records), though several complicated moisture processes affect the seasonal variability in $\delta^{18}O$ values in ice cores and cave speleothems (Dayem et al., 2010; Yao et al., 2013). Here we use the summer insolation at 30°N (Berger and Loutre, 1991) and $\delta^{18}O$ records from the Guliya ice core on the TP (Thompson et al., 1997) as proxies for the temperature change, and the speleothem $\delta^{18}O$ Indian summer monsoon records from the Dongge, Yamen, Xiaobailong, Timta, and Bitto caves (Yuan et al., 2004; Sinha et al., 2005; Yang et al., 2010; Cai et al., 2015; Kathayat et al., 2016) as proxies for precipitation variability in the region (Fig. 7). The proxy chronologies are defined by using the dating methods of ^{14}C, ^{36}Cl, ^{230}Th, and orbital tuning, and the proxy errors are typically less than 5%. More information about the quality and associated errors of each proxy is provided in the original publications. In Figure 7, the temperature proxy records show that the temperature was progressively increasing from GS-2a to GI-1, and then dropped in GS-1. The speleothem $\delta^{18}O$ records indicate that the precipitation from the Indian summer monsoon was increasing from GS-2a to GI-1, and then decreasing in GS-1. Moreover, in the speleothem Indian summer monsoon records, the average $\delta^{18}O$ value in GI-1 approximates to the past 1000 year $\delta^{18}O$ value, and the values in GS-2a and GS-1 were higher than the past 1000 year $\delta^{18}O$ value (Supplementary Table S4). Assuming a linear relationship between speleothem $\delta^{18}O$ and precipitation, it can be deduced that the precipitation values in GS-2a, GI-1, and GS-1 were 60%–70%, 100%, and 80%–90%, respectively, of the value for the past 1000 years. From the modeling results, these precipitation reductions require temperature drops of 2.6°C–2.9°C, ∼1.6°C, and 1.4°C–1.5°C to reproduce the PM1, PM2, and PM3 glacial extents, respectively. This suggests that a warming trend from the PM1 to PM3 glacial events could have dominated the glacier's receding during the last glacial termination, with the corresponding ELAs lower by ∼300, ∼250, and ∼190 m relative to the modern ELA of ∼5730 m. We acknowledge that a more specific climate inference is difficult until more accurate temperature or precipitation proxies are available for the three glacial events. However, in the Samdainkangsang Peak region, Xu et al. (2017b) also suggested that a temperature drop of 2.6°C–2.8°C and 60%–70% of modern (1981–2010) precipitation can support the late-glacial (GS-2a) glacial extents in the Barenduo valley, based on reconstructions of the late-glacial glacial extents in the valley. Due to lack of other quantitative climate constraints for the GI-1 and GS-1 glacial events, it is impossible to make a full comparison of the modeled climate scenarios in the region.

Climatic relationships with oceanic and atmospheric circulations

During the last glacial termination, meltwater and iceberg outbursts from the margins of the NH ice sheets led to the glacial stadials of GS-2a (Heinrich 1) and GS-1 (Younger Dryas) in the North Atlantic region by reducing the thermohaline circulation (THC). A substantial drop in sea-surface temperature continued during the GS-2a and GS-1 periods in the region (Naughton et al., 2009). This resulted in an expansion of winter sea ice and introduced a highly seasonal climate in the region (Denton et al., 2005), because the spread of winter sea ice created Siberia-like conditions, dominated by large temperature differences between winter and summer in the North Atlantic region. This explains why the mean annual temperatures in Greenland and northern Europe decreased

https://doi.org/10.1017/qua.2020.7 Published online by Cambridge University Press

by 12°C to 17°C relative to today's values in GS-1, with a 22°C to 28°C decrease in winter and a 3°C to 6°C decrease in summer (Denton et al., 2005, 2010). Although the HTC also controlled the Indian Ocean (where the Indian summer monsoon transports water vapor to the TP) for a major portion of the last glacial termination (Naik et al., 2019; Sun et al., 2019), our estimated GS-1 temperature depression of 1.4°C–1.5°C for the Qiongmu Gangri peak is much less than the values from the North Atlantic region. This argument is in agreement with the view of Rehfeld et al. (2018) that the temperature decrease from the LGM to Holocene had a clear zonal pattern, with a progressive reduction in change from the high latitudes toward the tropics.

Using a global atmospheric circulation model, Barnett et al. (1988) related weakened Asian monsoons to long and cold high-latitude winters, similar to a consequence of the winter sea-ice cover in the North Atlantic. Chiang and Bitz (2005), using a Community Climate Model (version 3), also illustrated that the Intertropical Convergence Zone (ITCZ) shifted southward with an imposed increased ice cover anomaly like that of the North Atlantic during GS-2a. Model results therefore suggest that the expansion of sea ice across the North Atlantic, particularly in winter, was probably the key factor in spreading the impacts of the millennial-scale cold events throughout the NH and into midlatitudinal regions (Denton et al., 2010) such as the TP. In addition, the cooling in the North Atlantic region during GS-2a might have increased the latitudinal temperature gradient in the NH. This then increased the meridional atmospheric pressure gradient and thus strengthened the westerlies, because the westerlies are formed by the air movement transition from meridional to zonal under the Coriolis force. The strengthened westerlies could have brought cold air into the TP. Consequently, during GS-2a, the cold westerlies and weak Indian summer monsoon dominated the TP, and thus the Qiongmu Gangri peak region was affected by cool and dry conditions. Moreover, by analyzing temperature proxy data from the Arabian Sea and climate model simulations, Tierney et al. (2016) suggested that during GS-2a, the sea-surface cooling in the Indian Ocean was a critical link between the North Atlantic event and the Indian monsoon failure.

The warmer and wetter conditions of the GI-1 period can be attributed to the enhanced THC, with the ITCZ shifting northward and thus the Indian summer monsoon being strengthened (Sinha et al., 2005; Liu et al., 2009; Banakar et al., 2017). Despite the relatively warmer conditions in the GI-1 period, it still appeared to be colder relative to the GS-1 period in the Qiongmu Gangri peak region, as evidenced by our glacier–climate modeling on the basis of the greater glacial extent of PM2 than PM3. This warming trend from GS-2a through GI-1 to GS-1, especially the less marked GS-1 signature, is also similar to the modeled temperature trend (Liu et al., 2009; Tierney et al., 2016) and the chironomid-based temperature reconstruction in southwestern China (Zhang et al., 2019). This pattern follows more closely the long increase in the NH summer insolation during the last glacial termination (Fig. 7), suggesting that the influence of the North Atlantic millennial-scale cold events on the TP declined as the last glacial termination progressed. Zhang et al. (2019) also proposed that during the last glacial termination, there was a progressive increase in Indian summer monsoon influence on climate change in southwestern China. Furthermore, using a pollen discrimination index, Zhu et al. (2015) suggested that the Lake Nam Co area, ~70 km northeast of the Qiongmu Gangri peak, was influenced by the Indian summer monsoon in the GS-1 period, although other lake-sediment proxies indicated a drier climate relative to the GI-1 period in the region. They also argued that because of the limited temperature decrease in the north Indian Ocean upwelling through the THC in the GS-1 period, the Indian summer monsoon was still dominant in the north Indian Ocean, Indian subcontinent, and even farther north, although the THC might have been weak during this period.

These patterns of oceanic and atmospheric circulations are consistent with our climate inferences using glacier–climate modeling. This suggests that the glacial events on the TP during the last glacial termination can be well correlated with the millennium-scale climate events in the North Atlantic region driven by the westerlies, and the Indian summer monsoon played a positive role in sustaining the glaciers under a warming climate trend in the region.

CONCLUSION

Using cosmogenic ^{10}Be exposure dating and glacial modeling methods, we constrained the timing and climatic conditions for the late-glacial glacial events in the Pagele valley, Qiongmu Gangri peak, southern TP. Three lateral-frontal moraines (PM1, PM2, and PM3) were found to terminate at elevations of 5170, 5200, and 5230 m asl, respectively. These moraines indicate the glacier retreated about 1000 m from the PM1 to PM3, and the glacier's length was 3500 m at the PM1. After outliers are discarded, the mean (15,850 ± 980, 14,140 ± 880, and 12,430 ± 790 yr) and the oldest ages (16,190 ± 1000, 14,710 ± 910, and 12,980 ± 820 yr) from each of the three moraines all suggest that the PM1, PM2, and PM3 moraines respectively correspond well with the GS-2a (or Heinrich 1), GI-1 (or Bølling-Allerød), and GS-1 (or Younger Dryas) events in the Greenland ice-core record. The PM1 and PM3 moraines can be correlated to the late-glacial moraine found in the Barenduo valley and the Yanbajian inner moraine of the region, respectively (Owen et al., 2005; Chevalier et al., 2011). Using the glacier–climate model, we showed that the glacier had areas of 12.6, 11.6, and 10.9 km^2 and volumes of 1.03–1.14, 0.79–0.88, and 0.61–0.68 km^3 at the PM1, PM2, and PM3 moraine positions, respectively. Possible climatic scenarios of temperature and precipitation have also been established to support these three glacial extents. Considering more realistic precipitation values of 60%–80%, ~100%, and 80%–90% of present value, the model results indicated that the temperature in the region decreased by 2.6°C–2.9°C, ~1.6°C, and 1.4°C–1.5°C during the GS-2a, GI-1, and GS-1 periods,

https://doi.org/10.1017/qua.2020.7 Published online by Cambridge University Press

respectively. The temperature drop of 2.6°C–2.9°C in GS-2a is also compatible with the climatic reconstruction (2.6°C–2.8°C) for the late glacial in the Barenduo valley (Xu et al., 2017b).

Taken together with information from oceanic and atmospheric circulations, these results imply that on the TP, the glacial events during the last glacial termination are well correlated with the millennium-scale climate events in the North Atlantic region by the westerlies, and the Indian summer monsoon plays a positive role in sustaining the glaciers under the warming climate trend. Therefore, any explanation for the relationship between glacier and climate during the last glacial termination on the TP must consider the interactions between the westerlies and the India summer monsoon in the region.

ACKNOWLEDGMENTS

This research was funded by the Second Tibetan Plateau Scientific Expedition and Research Program (STEP, 2019QZKK0101), National Natural Science Foundation of China (NSFC, grant no. 41771019), Strategic Priority Research Program (A) of the Chinese Academy of Sciences (XDA2007010201). We thank Jing Wei for processing the ^{10}Be samples and Zhang Qian and Wu Yubin for their help in collecting boulder samples. Also, we would like to thank M.-L. Chevalier, the anonymous reviewer, J. Schulmeister (associate editor), and L. Owen (senior editor) for their suggestions and comments, which greatly improved the article.

SUPPLEMENTARY MATERIAL

The supplementary material for this article can be found at https://doi.org/10.1017/qua.2020.7.

REFERENCES

Balco, G., Stone, J.O., Lifton, N.A., Dunai, T.J., 2008. A complete and easily accessible means of calculating surface exposure ages or erosion rates from ^{10}Be and ^{26}Al measurements. *Quaternary Geochronology* 8, 174–195.

Banakar, V.K., Baidya, S., Piotrowski, A.M., Shankar, D., 2017. Indian summer monsoon forcing on the deglacial polar cold reversals. *Journal of Earth System Science* 126, 87.

Barnett, T.P., Dümenil, L., Schlese, U., Roeckner, E., 1988. The effect of Eurasian snow cover on global climate. *Science* 239, 504–507.

Benn, D.I., Owen, L.A., 1998. The role of the Indian summer monsoon and the mid-latitude westerlies in Himalayan glaciation: review and speculative discussion. *Journal of the Geological Society* 155, 353–363.

Berger, A.M., Loutre, F., 1991. Insolation values for the climate of the last 10 million years. *Quaternary Science Reviews* 10, 297–314.

Björck, S., Walker, M.J.C., Cwynar, L.C., Johnsen, S., Knudsen, K.-L., Lowe, J.J., Wohlfarth, B., INTIMATE Members, 1998. An event stratigraphy for the Last Termination in the North Atlantic region based on the Greenland ice-core record: a proposal by the INTIMATE group. *Journal of Quaternary Science* 13, 283–292.

Blomdin, R., Stroeven, A. P., Harbor, J. M., Lifton, N. A., Heyman, J., Gribenski, N., Petrakov, D. A., *et al*., 2016. Evaluating the timing of former glacier expansions in the Tian Shan: A key step towards robust spatial correlations. *Quaternary Science Reviews* 153, 78–96.

Broecker, W.S., van Donk, J., 1970. Insolation changes, ice volume, and the ^{18}O record in deep-sea cores. *Reviews of Geophysics* 8, 169–198.

Cai, Y., Fung, I.Y., Edwards, R.L., An, Z., Cheng, H., Lee, J.-E., Tan, L., *et al*.., 2015. Variability of stalagmite-inferred Indian monsoon precipitation over the past 252,000 y. *Proceedings of the National Academy of Sciences USA* 112, 2954–2959.

Chevalier, M.-L., Hilley, G., Tapponnier, P., Van Der Weord, J., Liu-Zeng, J., Finkel, R.C., Ryerson, F.J., Li, H., Liu, X., 2011. Constrains on the late Quaternary glaciations in Tibet from cosmogenic exposure ages of moraine surface. *Quaternary Science Reviews* 30, 528–554.

Chiang, J.C.H., Bitz, C.M., 2005. Influence of high latitude ice cover on the marine Intertropical Convergence Zone. *Climate Dynamics* 25, 477–496.

Cuffey, K.M., Paterson, W.S.B., 2010. *The Physics of Glaciers*. 4th ed. Elsevier, Boston.

Dayem, K.E., Molnar, P., Battisti, D.S., Roe, G.H., 2010. Lessons learned from oxygen isotopes in modern precipitation applied to interpretation of speleothem records of paleoclimate from eastern Asia. *Earth and Planetary Science Letters* 295, 219–230.

Denton, G.H., Alley, R.B., Comer, G.C., Broecker, W.S., 2005. The role of seasonality in abrupt climate change. *Quaternary Science Reviews* 24, 1159–1182.

Denton, G.H., Anderson, R.F., Toggweiler, J.R., Edwards, R.L., Schaefer, J.M., Putnam, A.E., 2010. The last glacial termination. *Science* 328, 1652–1656.

Dong, G., Xu, X., Zhou, W., Fu, Y., Zhang L., Li M., 2017. Cosmogenic ^{10}Be surface exposure dating and glacier reconstruction for the Last Glacial Maximum in the Quemuqu Valley, western Nyainqentanglha Mountains, south Tibet. *Journal of Quaternary Science* 32, 639–652.

Dortch, J.M., Owen, L.A., Caffee, M.W., 2013. Timing and climatic drivers for glaciation across semi-arid western Himalayan-Tibetan orogen. *Quaternary Science Reviews* 78, 188–208.

Dortch, J.W., Owen, L.A., Haneberg, W.C., Caffee, M.W., Dietsch, C., Kamp, U., 2009. Nature and timing of large landslides in the Himalaya and Transhimalaya of northern India. *Quaternary Science Reviews* 28, 1037–1054.

Farinotti, D., Huss, M., Fürst, J.J., Landmann, J., Machguth, H., Maussion, F., Pandit, A., 2019. A consensus estimate for the ice thickness distribution of all glaciers on Earth. *Nature Geoscience* 12, 168–173.

Heyman, J., 2014. Paleoglaciation of the Tibetan Plateau and surrounding mountains based on exposure ages and ELA depression estimates. *Quaternary Science Reviews* 91, 30–41.

Heyman, J., Stroeven, A.P., Harbor, J., Caffee, M.W., 2011. Too young or too old: evaluating cosmogenic exposure dating based on an analysis of compiled boulder exposure ages. *Earth and Planetary Science Letters* 302, 71–80.

Kathayat, G., Cheng, H., Sinha, A., Spötl, C., Edwards, R.L., Zhang, H., Li, X., *et al*.., 2016. Indian monsoon variability on millennial-orbital timescales. *Scientific Reports* 6, 24374.

Kohl, C.P., Nishiizumi, K., 1992. Chemical isolation of quartz for measurement of in situ produced cosmogenic nuclides. *Geochimica et Cosmochimica Acta* 56, 3583–3587.

Laabs, B.J.C., Plummer, M.A., Mickelson, D.M., 2006. Climate during the last glacial maximum in the Wasatch and southern Uinta Mountains inferred from glacier modelling. *Geomorphology* 75, 300–317.

Lal, D., 1991. Cosmic ray labeling of erosion surfaces: in situ nuclide production rates and erosion models. *Earth and Planetary Science Letters* 104, 429–439.

Lana, B., Nakawo, M., Fukushima, Y., Ageta, Y., 1997. Application of a conceptual precipitation-runoff model (HYCYMODEL) in a debris-covered glacierized basin in the Langtang Valley, Nepal Himalaya. *Annals of Glaciology* 25, 226–231.

Li, Y.K., 2013. Determining topographic shielding from digital elevation models for cosmogenic nuclide analysis: a GIS approach and field validation. *Journal of Mountain Science* 10, 355–362.

Lifton, N.A., Sato, T., Dunai, T.J., 2014. Scaling in situ cosmogenic nuclide production rates using analytical approximations to atmospheric cosmic-ray fluxes. *Earth and Planetary Science Letters* 386, 149–160.

Liu, Z., Otto-Bliesner, B.L., He, F., Brady, E.C., Tomas, R., Clark, P.U., Carlson, A.E., *et al*., 2009. Transient simulation of last deglaciation with a new mechanism for Bølling-Allerød warming. *Science* 325, 310–313.

Mihalcea, C., Mayer, C., Diolaiuti, G., D'Agata, C., Smiraglia, C., Lambrecht, A., Vuiller-moz, E., Tartari, G., 2008. Spatial distribution of debris thickness and melting from remote-sensing and meteorological data, at debris-covered Baltoro glacier, Karakoram, Pakistan. *Annals of Glaciology* 48, 49–57.

Molnar, P., England, P., 1990. Late Cenozoic uplift of mountainranges and global climate change: chicken or egg? *Nature* 346, 29–34.

Murari, M.K., Owen, L.A., Dortch, J.M., Caffee, M.W., Dietsch, C., Fuchs, M., Haneberg, W.C., Sharma, M.C., Townsend-Small, A., 2014. Timing and climatic drivers for glaciation across monsoon-influenced regions of the Himalayan-Tibetan orogeny. *Quaternary Science Reviews* 88, 159–182.

Naik, S.S., Basak, C., Goldstein, S.L., Naidu, P.D., Naik, S.N., 2019. A 16-kyr record of ocean circulation and monsoon intensification from the central Bay of Bengal. *Geochemistry, Geophysics, Geosystems* 20, 872–882.

Naughton, F., Sánchez Goñi, M.F., Kageyama, M., Bard, E., Duprat, J., Cortijo, E., Desprat, S., *et al*., 2009. Wet to dry climatic trend in north-western Iberia within Heinrich events. *Earth and Planetary Science Letters* 284, 329–342.

Nicholson, L., Benn, D., 2006. Calculating ice melt beneath a debris layer using meteorological data. *Journal of Glaciology* 52, 463–470.

Nishiizumi, K., Imamura, M., Caffee, M.W., Southon, J.R., Finkel, R.C., McAninch, J., 2007. Absolute calibration of ^{10}Be AMS standards. *Nuclear Instruments and Methods in Physics Research Section B* 258, 403–413.

Owen, L.A., Caffee, M.W., Finkel, R.C., Seong Y.B., 2008. Quaternary glaciation of the Himalayan-Tibetan orogen. *Journal of Quaternary Science* 23, 513–531.

Owen, L.A., Dortch, J.M., 2014. Nature and timing of Quaternary glaciation in the Himalayan-Tibetan orogeny. *Quaternary Science Reviews* 88, 14–54.

Owen, L.A., Finkel, R.C., Barnard, P.L., Haizhou, M., Asahi, K., Caffee, M.W., Derbyshire, E., 2005. Climatic and topographic controls on the style and timing of Late Quaternary glaciation throughout Tibet and the Himalaya defined by ^{10}Be cosmogenic radionuclide surface exposure dating. *Quaternary Science Reviews* 24, 1391–1411.

Peirce, B., 1852. Criterion for the rejection of doubtful observations. *Astronomical Journal* 2, 161–163.

Plummer, M.A., 2002. *Paleoclimate Conditions during the Last Deglaciation Inferred from Combined Analysis of Pluvial and Glacial Records*. Ph.D. thesis, New Mexico Institute of Mining and Technology, Socorro, NM. pp. 346.

Plummer, M.A., Phillips, F.M., 2003. A 2-D numerical model of snow/ice energy balance and ice flow for paleoclimatic interpretation of glacial geomorphic features. *Quaternary Science Reviews* 22, 1389–1406.

Prell, W.L., Kutzbach, J.E. 1992. Sensitivity of the Indian monsoon to forcing parameters and implications for its evolution. *Nature* 360, 647–652.

Pu, J., Yao, T., Duan, K., 2003. An observation on surface ablation on the Yangbark glacier in the Muztag Ata, China. [In Chinese with English abstract.] *Journal of Glaciology and Geocryology* 25, 680–684.

Rasmussen, S.O., Andersen, K.K., Svensson, A.M., Steffensen, J.P., Vinther, B.M., Clausen, H.B., Siggaard-Andersen, M.-L., *et al*., 2006. A new Greenland ice core chronology for the last glacial termination. *Journal of Geophysical Research* 111, D06102.

Raymo, M.E., Ruddiman, W.F. 1992. Tectonic forcing of late Cenozoic climate. *Nature* 359, 117–124.

Rehfeld, K., Münch, T., Ho, S.L., Laepple, T., 2018. Global patterns of declining temperature variability from the Last Glacial Maximum to the Holocene. *Nature* 554, 356–359.

Ressen, H., Isarin, R.F.B., 2001. The two major warming phases of the last deglaciation at ∼14.7 and ∼11.5 ka cal BP in Europe: climate reconstructions and AGCM experiments. *Global and Planetary Change* 30, 117–153.

Schaefer, J.M., Denton, G.H., Kaplan, M., Putnam, A., Finkel, R.C., Barrell, D.J.A., Andersen, B.G., *et al*., 2009. High-frequency Holocene glacier fluctuations in New Zealand differ from the northern signature. *Science* 324, 622–625.

Sinha, A., Cannariato, K.G., Stott, L.D., Li, H., You, C., Chen, H., Edwards, R.L., Singh, I.B., 2005. Variability of Southwest Indian summer monsoon precipitation during the Bølling-Allerød. *Geology* 33, 813–816.

Stone, J.O., 2000. Air pressure and cosmogenic isotope production. *Journal of Geophysical Research* 105, 23753–23759.

Sun, W., Zhang, E., Shulmeister, J., Bird, M.I., Chang, J., Shen, J., 2019. Abrupt changes in Indian summer monsoon strength during the last deglaciation and early Holocene based on stable isotope evidence from Lake Chenghai, southwest China. *Quaternary Science Reviews* 218, 1–9.

Thackray, G.D., Owen, L.A., Yi, C.L., 2008. Timing and nature of late Quaternary mountain glaciation. *Journal of Quaternary Science* 23, 503–508.

Thompson, L.G., Yao, T., Davis, M.E., Henderson, K.A., Mosley-Thompson, E., Lin, P., Beer, J., Synal, H., Cole-Dai, J., Bolzan, J.F., 1997. Tropical climate instability: the Last Glacial Cycle from a Qinghai-Tibetan ice core. *Science* 276, 1821–1825.

Tierney, J.E., Pausata, F.S.R., de Menocal, P., 2016. Deglacial Indian monsoon failure and North Atlantic stadials linked by Indian Ocean surface. *Nature Geoscience* 9, 46–50.

Xu, X., Dong, G., Pan, B., Hu, G., Bi, W., Liu, J., Yi, C., 2017b. Late Glacial glacier-climate modeling in two valleys on the eastern slope of Samdainkangsang Peak, Nyaiqentanggulha Mountains. *Science China Earth Sciences* 60, 135–162.

Xu, X., Hu, G., Qiao, B., 2013. Last Glacial Maximum climate based on cosmogenic ^{10}Be exposure ages and glacier modeling for the head of Tashkurgan Valley, northwest Tibetan Plateau. *Quaternary Science Reviews* 80, 91–101.

Xu, X., Pan, B., Dong, G., Yi, C., Glasser, N.F., 2017a. Last Glacial climate reconstruction by exploring glacier sensitivity to climate

https://doi.org/10.1017/qua.2020.7 Published online by Cambridge University Press

on the southeastern slope of the western Nyaiqentanglha Shan, Tibetan Plateau. *Journal of Glaciology* 63, 361–371.

Yang, Y., Yuan, D.X., Cheng, H., Zhang, M.L., Qin, J.M., Lin, Y.S., Zhu, X.Y., Edwards, R.L., 2010. Precise dating of abrupt shifts in the Asian Monsoon during the last deglaciation based on stalagmite data from Yamen Cave, Guizhou Province, China. *Science China Earth Sciences* 53, 633–641.

Yao, T.D., Masson-Delmotte, V., Gao, J., Yu, W., Yang, X., Risi, C., Sturm, C., *et al*.., 2013. A review of climatic controls on $\delta^{18}O$ in precipitation over the Tibetan Plateau: observations and simulations. *Reviews of Geophysics* 51, 525–548.

Young, N.E., Briner, J.P., Schaefer, J., Zimmerman, S., Finkel, R.C., 2019. Early Younger Dryas glacier culmination in southern Alaska: implications for North Atlantic climate change during the last deglaciation. *Geology* 47, 550–554.

Yuan, D., Cheng, H., Edwards, R.L., Dykoski, C.A., Kelly, M.J., Zhang, M., Qing, J., *et al*., 2004. Timing, duration, and transitions of the last interglacial Asian monsoon. *Science* 304, 575–578.

Zech, R., Zech, M., Kubik, P.W., Kharki, K., Zech, W., 2009. Deglaciation and landscape history around Annapurna, Nepal, based on ^{10}Be surface exposure dating. *Quaternary Science Reviews* 28, 1106–1118.

Zhang, E., Chang, J., Shulmeister, J., Langdon, P., Sun, W., Cao, Y., Yang, X., Shen, J., 2019. Summer temperature fluctuations in Southwestern China during the end of the LGM and the last deglaciation. *Earth and Planetary Science Letters* 509, 78–87

Zhang, Y., Li, B., Zheng, D., 2002. A discussion on the boundary and area of the Tibetan Plateau in China. *Geographical Research* 21, 1–8.

Zheng, B., Xu, Q., Shen, Y., 2002. The relationship between climate change and Quaternary glacial cycles on the Qinghai-Tibetan Plateau: review and speculation. *Quaternary International* 97/98, 93–101.

Zhu, L., Lü, X., Wang, J., Peng, P., Kasper, P., Daut, G., Haberzettl, T., *et al*.., 2015. Climate change on the Tibetan Plateau in response to shifting atmospheric circulation since the LGM. *Scientific Reports* 5, 13318.